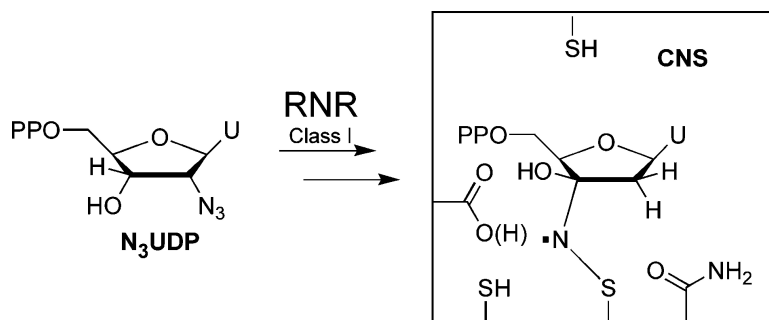


## Structure of the Nitrogen-Centered Radical Formed during Inactivation of *E. coli* Ribonucleotide Reductase by 2'-Azido-2'-deoxyuridine-5'-diphosphate: Trapping of the 3'-Ketonucleotide

Jrg Fritscher, Erin Artin, Stanislaw Wnuk, Galit Bar, John H. Robblee, Sylwia Kacprzak, Martin Kaupp, Robert G. Griffin, Marina Bennati, and JoAnne Stubbe

*J. Am. Chem. Soc.*, **2005**, 127 (21), 7729-7738 • DOI: 10.1021/ja043111x • Publication Date (Web): 10 May 2005

Downloaded from <http://pubs.acs.org> on March 25, 2009



### More About This Article

Additional resources and features associated with this article are available within the HTML version:

- Supporting Information
- Links to the 6 articles that cite this article, as of the time of this article download
- Access to high resolution figures
- Links to articles and content related to this article
- Copyright permission to reproduce figures and/or text from this article

[View the Full Text HTML](#)

### Structure of the Nitrogen-Centered Radical Formed during Inactivation of *E. coli* Ribonucleotide Reductase by 2'-Azido-2'-deoxyuridine-5'-diphosphate: Trapping of the 3'-Ketonucleotide

Jörg Fritscher,<sup>‡</sup> Erin Artin,<sup>†</sup> Stanislaw Wnuk,<sup>§</sup> Galit Bar,<sup>†</sup> John H. Robblee,<sup>†</sup> Sylwia Kacprzak,<sup>¶</sup> Martin Kaupp,<sup>¶</sup> Robert G. Griffin,<sup>†</sup> Marina Bennati,<sup>\*,‡</sup> and JoAnne Stubbe<sup>\*,†</sup>

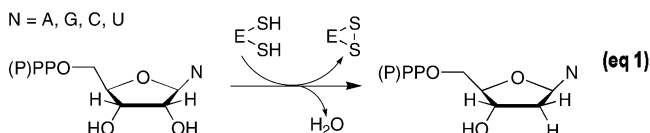
Contribution from the Department of Chemistry, Massachusetts Institute of Technology, Cambridge, Massachusetts 02139, Institute of Physical and Theoretical Chemistry, J. W. Goethe University of Frankfurt, and Center for Biological Magnetic Resonance, 60439 Frankfurt, Germany, Department of Chemistry, Florida International University, Miami, Florida 33199, and Institute of Inorganic Chemistry, J. Maximilians University of Würzburg, 97074 Würzburg, Germany

Received November 16, 2004; E-mail: bennati@chemie.uni-frankfurt.de; stubbe@mit.edu

**Abstract:** Ribonucleotide reductases (RNRs) catalyze the conversion of nucleotides to deoxynucleotides providing the monomeric precursors required for DNA replication and repair. The class I RNRs are composed of two homodimeric subunits: R1 and R2. R1 has the active site where nucleotide reduction occurs, and R2 contains the diiron tyrosyl radical (Y•) cofactor essential for radical initiation on R1. Mechanism-based inhibitors, such as 2'-azido-2'-deoxyuridine-5'-diphosphate (N<sub>3</sub>UDP), have provided much insight into the reduction mechanism. N<sub>3</sub>UDP is a stoichiometric inactivator that, upon interaction with RNR, results in loss of the Y• in R2 and formation of a nitrogen-centered radical (N•) covalently attached to C225 (R-S-N•-X) in the active site of R1. N<sub>2</sub> is lost prior to N• formation, and after its formation, stoichiometric amounts of 2-methylene-3-furanone, pyrophosphate, and uracil are also generated. On the basis of the hyperfine interactions associated with N•, it was proposed that N• is also covalently attached to the nucleotide through either the oxygen of the 3'-OH (R-S-N•-O-R') or the 3'-C (R-S-N•-C-OH). To distinguish between the proposed structures, the inactivation was carried out with 3'-[<sup>17</sup>O]-N<sub>3</sub>UDP and N• was examined by 9 and 140 GHz EPR spectroscopy. Broadening of the N• signal was detected and the spectrum simulated to obtain the [<sup>17</sup>O] hyperfine tensor. DFT calculations were employed to determine which structures are in best agreement with the simulated hyperfine tensor and our previous ESEEM data. The results are most consistent with the R-S-N•-C-OH structure and provide evidence for the trapping of a 3'-ketonucleotide in the reduction process.

#### Introduction

Ribonucleotide reductases (RNRs) catalyze an essential step in DNA replication and repair, conversion of nucleotides to deoxynucleotides (eq 1), by providing the monomeric precursors required for these processes.<sup>1–3</sup>



The class I RNRs are proposed to be composed of a 1:1 mixture of two homodimeric subunits: R1 and R2.<sup>4,5</sup> R1 is the

business end of the RNR containing the active site with three cysteines essential for catalysis<sup>6–11</sup> and allosteric sites that govern substrate specificity and turnover rate.<sup>12–15</sup> Two additional cysteines in the C-terminus of R1 are required to reduce

<sup>†</sup> Massachusetts Institute of Technology.

<sup>‡</sup> J. W. Goethe University of Frankfurt.

<sup>§</sup> Florida International University.

<sup>¶</sup> J. Maximilians University of Würzburg.

(1) Licht, S.; Stubbe, J. In *Comprehensive Natural Products Chemistry*; Barton, S. D., Nakanishi, K., Meth-Cohn, O., Poulter, C. D., Eds.; Elsevier Science: New York, 1999; Vol. 5, p 163.

- (2) Eklund, H.; Uhlin, U.; Farnegardh, M.; Logan, D. T.; Nordlund, P. *Prog. Biophys. Mol. Biol.* **2001**, *77*, 177–268.
- (3) Zhou, B. B. S.; Elledge, S. J. *Nature* **2000**, *408*, 433–439.
- (4) Thelander, L. *J. Biol. Chem.* **1973**, *248*, 4591–4601.
- (5) Brown, N. C.; Reichard, P. *J. Mol. Biol.* **1969**, *46*, 25–38.
- (6) Lin, A. N.; Ashley, G. W.; Stubbe, J. *Biochemistry* **1987**, *26*, 6905–6909.
- (7) Aberg, A.; Hahne, S.; Karlsson, M.; Larsson, A.; Ormo, M.; Ahgren, A.; Sjöberg, B. M. *J. Biol. Chem.* **1989**, *264*, 12249–12252.
- (8) Mao, S. S.; Johnston, M. I.; Bollinger, J. M.; Stubbe, J. *Proc. Natl. Acad. Sci. U.S.A.* **1989**, *86*, 1485–1489.
- (9) Mao, S. S.; Holler, T. P.; Yu, G. X.; Bollinger, J. M., Jr.; Booker, S.; Johnston, M. I.; Stubbe, J. *Biochemistry* **1992**, *31*, 9733–9743.
- (10) Mao, S. S.; Holler, T. P.; Bollinger, J. M., Jr.; Yu, G. X.; Johnston, M. I.; Stubbe, J. *Biochemistry* **1992**, *31*, 9744–9751.
- (11) Mao, S. S.; Yu, G. X.; Chalfoun, D.; Stubbe, J. *Biochemistry* **1992**, *31*, 9752–9759.
- (12) Brown, N. C.; Reichard, P. *J. Mol. Biol.* **1969**, *46*, 39–55.
- (13) Thelander, L.; Reichard, P. *Annu. Rev. Biochem.* **1979**, *48*, 133–158.
- (14) Kashlan, O. B.; Scott, C. P.; Lear, J. D.; Cooperman, B. S. *Biochemistry* **2002**, *41*, 462–474.
- (15) Kashlan, O. B.; Cooperman, B. S. *Biochemistry* **2003**, *42*, 1696–1706.

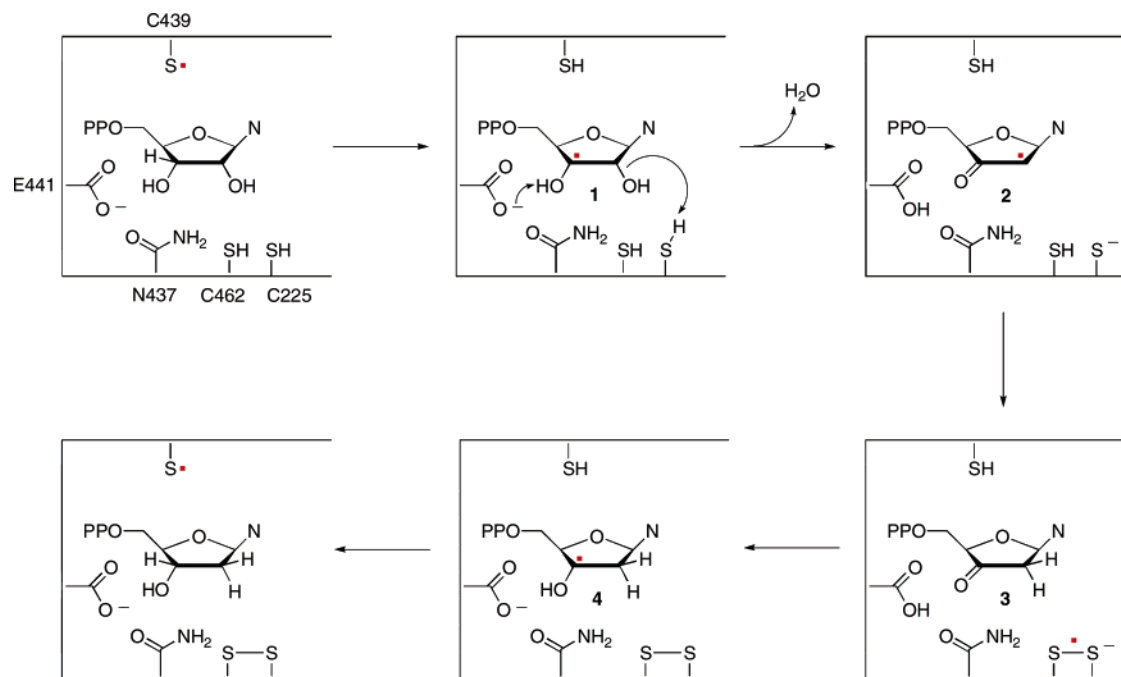


**Figure 1.** Mechanistic model for the reaction catalyzed by RNR. Only the active site of R1 is shown. The C439 S• is proposed to be generated by the Y• on R2. N = A, G, C, or U.

the active site disulfide in preparation for additional turnovers.<sup>6,7,9</sup> R2 contains the radical initiator, the diiron tyrosyl radical (Y•) cofactor.<sup>16</sup> This Y• is proposed to generate a thiyl radical (S•) in the active site on R1 that then initiates nucleotide reduction. The mechanism of nucleotide reduction has been studied for more than two decades using biochemical, chemical, and structural probes, resulting in the mechanistic model shown in Figure 1.

We have recently shown that the rate-determining step in *Escherichia coli* RNR is a physical step prior to generation of the putative S• on C439.<sup>17</sup> This has precluded detection of intermediates in the reduction process with the normal substrate. Perturbation of the system using mechanism-based inhibitors and site-directed mutants of R1 and R2 has provided the bulk of the insight into the reduction mechanism by inference. We now report electron paramagnetic resonance (EPR) spectroscopic studies on the interaction of 2'-azido-2'-deoxy-3'-[<sup>17</sup>O]-uridine-5'-diphosphate (3'-[<sup>17</sup>O]-N<sub>3</sub>UDP, **5**, Figure 2) with RNR. The EPR studies in conjunction with density functional theory (DFT) calculations reveal the structure of the nitrogen-centered radical (N•) generated during the inactivation of RNR by N<sub>3</sub>UDP. The results provide direct evidence for the trapping of a 3'-ketonucleotide **2** or **3** (Figure 2) in the reduction process.

EPR methods have been essential in the deconvolution of the complex mechanism of the ribonucleotide reduction process. For example, studies on the interaction of 2'-vinylfluorocytidine-5'-diphosphate with *E. coli* RNR demonstrated that the enzyme could generate a 3'-allyl nucleotide radical.<sup>18,19</sup> This experiment,

along with V/K isotope effects measured with 3'-[<sup>3</sup>H]-NDPs,<sup>20,21</sup> provided evidence that RNRs can abstract a 3'-hydrogen atom from a nucleotide substrate (**1**, Figure 1). Studies with an active site mutant of R1, E441Q, and substrate CDP resulted in conversion of the normal substrate into a putative 3'-ketodeoxynucleotide concomitant with the buildup of a disulfide radical anion (**3**, Figure 1).<sup>22</sup> The requirement for protonation of the 3'-ketone (**3**, Figure 1) to effect reduction by electron transfer from the disulfide radical anion<sup>23</sup> predicted the buildup of this intermediate when the proton source (E441) was removed.

Use of 2'-halogenated-2'-deoxynucleotides has provided evidence for a ketyl radical intermediate (**2**, Figure 1). 3'-[<sup>3</sup>H]-CIUDP upon incubation with RNR resulted in trapping of 2'-[<sup>3</sup>H]-3'-keto-2'-deoxynucleotide.<sup>24</sup> The location of the label and its stereochemistry were established after its reduction with NaBH<sub>4</sub>. Direct evidence for the 3'-ketodeoxynucleotide itself (**3**, Figure 1) has remained elusive.

2'-Azido-2'-deoxynucleoside-5'-diphosphates, N<sub>3</sub>NDPs, have been studied in detail since their discovery as potent inhibitors of RNRs by the Eckstein and Thelander groups in 1976.<sup>25</sup> These early studies revealed that incubation of RNRs with N<sub>3</sub>NDPs resulted in loss of the Y•. Subsequent studies revealed that this loss was accompanied by formation of a new nitrogen-centered radical (N•) and provided the first evidence for the involvement of nucleotide radicals in the reduction process.<sup>26,27</sup> Despite the wealth of knowledge about the interaction of this inhibitor with

(16) Sjöberg, B. M.; Reichard, P.; Graslund, A.; Ehrenberg, A. *J. Biol. Chem.* **1978**, *253*, 6863–6865.

(17) Ge, J.; Yu, G.; Ator, M. A.; Stubbe, J. *Biochemistry* **2003**, *42*, 10071–10083.

(18) Gerfen, G. J.; van der Donk, W. A.; Yu, G. X.; McCarthy, J. R.; Jarvi, E. T.; Matthews, D. P.; Farrar, C.; Griffin, R. G.; Stubbe, J. *J. Am. Chem. Soc.* **1998**, *120*, 3823–3835.

(19) van der Donk, W. A.; Gerfen, G. J.; Stubbe, J. *J. Am. Chem. Soc.* **1998**, *120*, 4252–4253.

(20) Stubbe, J.; Ackles, D. *J. Biol. Chem.* **1980**, *255*, 8027–8030.

(21) Stubbe, J.; Ator, M.; Krenitsky, T. *J. Biol. Chem.* **1983**, *258*, 1625–1631.

(22) Lawrence, C. C.; Bennati, M.; Obias, H. V.; Bar, G.; Griffin, R. G.; Stubbe, J. *Proc. Natl. Acad. Sci. U.S.A.* **1999**, *96*, 8979–8984.

(23) Lenz, R.; Giese, B. *J. Am. Chem. Soc.* **1997**, *119*, 2784–2794.

(24) Ator, M. A.; Stubbe, J. *Biochemistry* **1985**, *24*, 7214–7221.

(25) Thelander, L.; Larsson, B.; Hobbs, J.; Eckstein, F. *J. Biol. Chem.* **1976**, *251*, 1398–1405.

(26) Sjöberg, B. M.; Graslund, A.; Eckstein, F. *J. Biol. Chem.* **1983**, *258*, 8060–8067.

(27) Ator, M.; Salowe, S. P.; Stubbe, J.; Emptage, M. H.; Robins, M. J. *J. Am. Chem. Soc.* **1984**, *106*, 1886–1887.

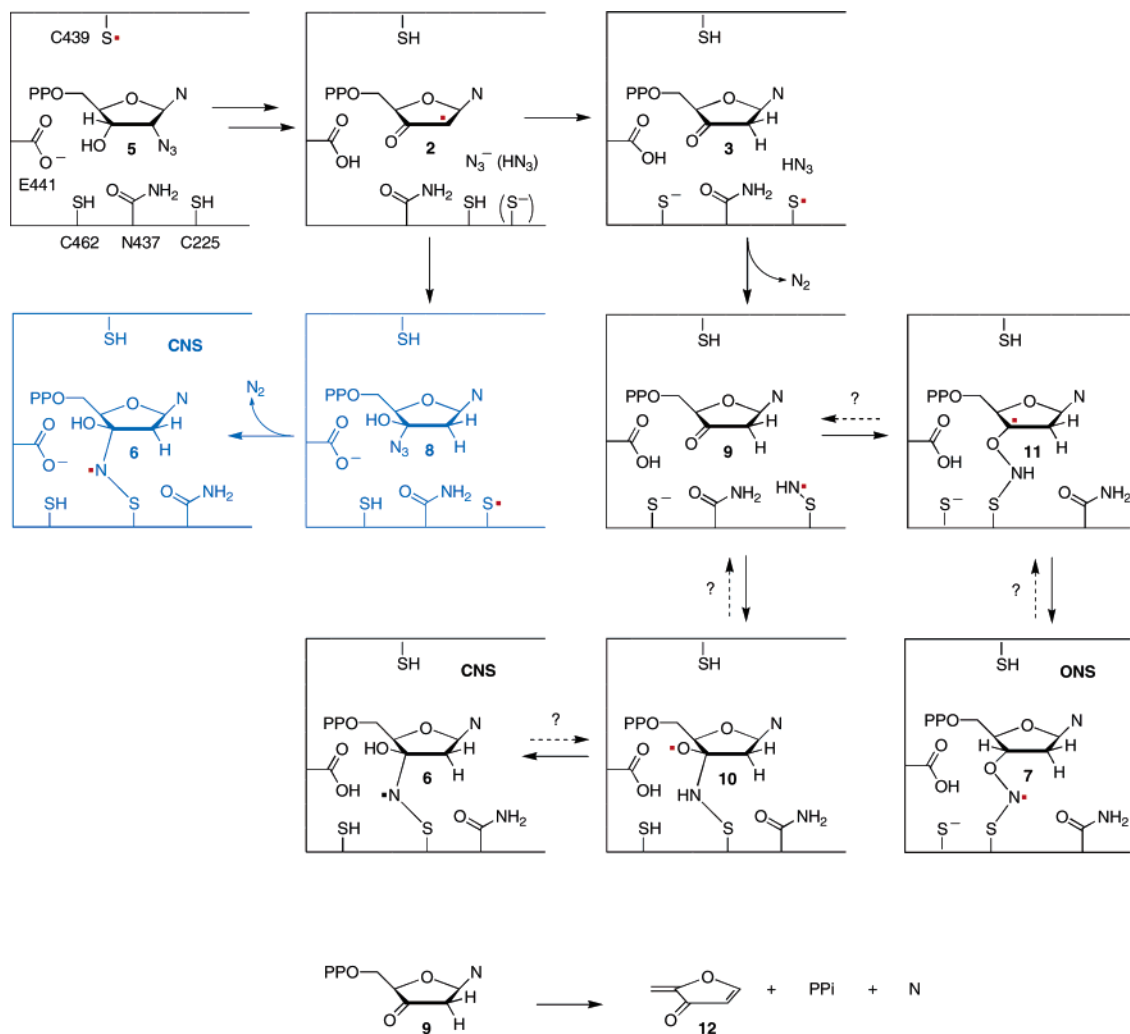


**Figure 2.** Two previously proposed structures for  $\text{N}\cdot$  (**6** and **7**) and pathways for their generation. The blue pathway is proposed based on theoretical studies,<sup>32</sup> while the black pathways were proposed by us.<sup>30</sup> The major differences involve the timing of  $\text{N}_2$  release and the role of E441.

RNR, the structure of the  $\text{N}\cdot$  has remained an issue.<sup>28–30</sup> Two options (structures **6** and **7**, Figure 2) have been considered based on isotopic labeling experiments using 1′-, 2′-, 3′-, 4′-[<sup>2</sup>H], [<sup>13</sup>C], and [<sup>15</sup>N] labeled  $\text{N}_3\text{UDP}$  and analysis of the resulting  $\text{N}\cdot$  by EPR and ESEEM spectroscopies at 9 and 140 GHz.<sup>29,30</sup> The availability of 3′-[<sup>17</sup>O]- $\text{N}_3\text{UDP}$ ,<sup>31</sup> in conjunction with DFT calculations, has now allowed us to distinguish between the two models and strongly supports **6** as the structure of the long-sought  $\text{N}\cdot$ .

We originally proposed two mechanistic options (Figure 2), both of which involve the sulfinylimine radical (**9**, Figure 2) interacting with a 3′-keto-2′-deoxynucleotide. The sulfinylimine radical was proposed to be generated directly by reaction of a thiyl radical on C225 with  $\text{HN}_3$  and to attack either the carbonyl carbon of the ketone directly (**9** to **10**, Figure 2) or the oxygen of the carbonyl group (**9** to **11**, Figure 2). The former mechanism was favored chemically, but the latter was more consistent with the ESEEM data. A recent theoretical study has proposed an

alternative mechanism to generate **6** (Figure 2).<sup>32</sup> In this mechanism, a released azide ion traps the ketyl radical **2** (Figure 2). This intermediate is then reduced by C225 to generate the corresponding thiyl radical. The thiyl radical then attacks the internal N of the azide to liberate  $\text{N}_2$  and generate **6** (Figure 2). Identification of the structure of  $\text{N}\cdot$  as **6** has now provided direct evidence for the trapping of a 3′-ketone, through either a ketyl radical **2** (Figure 2) or a 3′-keto-2′-deoxynucleotide **3** (Figure 2), depending on the timing of  $\text{N}_2$  release.

## Materials and Methods

Triethylamine (99% pure) was purchased from Acros, *N*-(2-hydroxyethyl)piperazine-*N'*-(2-ethanesulfonic acid) (HEPES) from US Biochemicals, and 1,4-dithiothreitol (DTT) from Mallinckrodt. DEAE Sephadex A-25 was purchased from Pharmacia. R1 and R2 were purified as previously described.<sup>29,33</sup> R1 ( $\epsilon_{280} = 189 \text{ mM}^{-1} \text{ cm}^{-1}$ ) had a specific activity of  $2100 \text{ nmol min}^{-1} \text{ mg}^{-1}$ , and R2 ( $\epsilon_{280} = 131 \text{ mM}^{-1} \text{ cm}^{-1}$ ) had a specific activity of  $6990 \text{ nmol min}^{-1} \text{ mg}^{-1}$ . R1 was pre-reduced prior to each experiment as previously reported.<sup>17</sup> *E. coli* TR was isolated from strain pTrX BL21 (DE3) and had a specific activity of  $40 \text{ units mg}^{-1}$ .<sup>34</sup> *E. coli* thioredoxin reductase (TRR) was isolated from strain pMR14 K91 and had a specific activity of  $1600 \text{ units mg}^{-1}$ .<sup>35</sup>

(28) Salowe, S. P.; Ator, M. A.; Stubbe, J. *Biochemistry* **1987**, *26*, 3408–3416.

(29) Salowe, S.; Bollinger, J. M., Jr.; Ator, M.; Stubbe, J.; McCracken, J.; Peisach, J.; Samano, M. C.; Robins, M. J. *Biochemistry* **1993**, *32*, 12749–12760.

(30) van der Donk, W. A.; Stubbe, J.; Gerfen, G. J.; Bellew, B. F.; Griffin, R. G. *J. Am. Chem. Soc.* **1995**, *117*, 8908–8916.

(31) Wnuk, S. F.; Chowdhury, S. M.; Garcia, P. I.; Robins, M. J. *J. Org. Chem.* **2002**, *67*, 1816–1819.

(32) Pereira, S.; Fernandes, P. A.; Ramos, M. J. *J. Comput. Chem.* **2004**, *25*, 227–237.

(33) Salowe, S. P.; Stubbe, J. *J. Bacteriol.* **1986**, *165*, 363–366.



$3'$ - $^{16}\text{O}$ - $\text{N}_3\text{UDP}$  was prepared from the nucleoside,  $2'$ -azido- $2'$ -deoxyuridine (Aldrich), as previously described.<sup>29</sup>  $3'$ - $^{17}\text{O}$ - $\text{N}_3\text{UDP}$  was prepared as described by Wnuk et al.<sup>31</sup> Mass spectra were recorded using the atmospheric pressure chemical ionization method in a positive mode using a Finnigan AQA Navigator. The percentage of  $^{17}\text{O}$  incorporation into  $3'$ - $^{17}\text{O}$ - $\text{N}_3\text{UDP}$  was  $46 \pm 2\%$ . All other chemicals were purchased from Sigma.

**Examination of the Reaction of  $\text{N}_3\text{UDP}$  and RNR by X-band EPR Spectroscopy.** Typical reactions contained in a final volume of 220  $\mu\text{L}$ : 0.75 mM TTP, 0.8 mM either  $3'$ - $^{16}\text{O}$ - or  $3'$ - $^{17}\text{O}$ - $\text{N}_3\text{UDP}$ , 90  $\mu\text{M}$  R1 (pre-reduced), 80  $\mu\text{M}$  R2, 50 mM HEPES (pH 7.6), 15 mM  $\text{MgSO}_4$ , 1 mM EDTA, 0.75 mM NADPH, 20  $\mu\text{M}$  TR, and 1  $\mu\text{M}$  TRR. All components except for the inhibitor were combined and equilibrated at 25 °C for 5 min. The reaction was started by the addition of the inhibitor and then transferred to an EPR tube where it was frozen in liquid nitrogen after 5 min incubation at 25 °C. A control sample with water replacing the inhibitor served as the standard for the amount of  $\text{Y}\bullet$ . EPR spectra at 9 GHz were acquired on a Bruker ESP-300 spectrometer equipped with a Bruker high-sensitivity 4419HS cylindrical cavity and an ER-041G microwave bridge containing an internal frequency counter. Spectra were acquired at 77 K using a liquid helium cooled ESR-900 cryostat and an Oxford LLT 650/1.0 transfer line. The parameters were as follows: microwave frequency for the  $3'$ - $^{16}\text{O}$ - and  $3'$ - $^{17}\text{O}$ - $\text{N}_3\text{UDP}$  samples was 9.389052 and 9.389072 GHz, respectively; microwave power 0.1 mW; modulation frequency 100 kHz; modulation amplitude 1 G; conversion time 20.48 ms; time constant 5.12 ms. For each sample, 100 scans were acquired with 2048 points per spectrum.

**Examination of the Reaction of  $\text{N}_3\text{UDP}$  and RNR by 140 GHz EPR Spectroscopy.** The reaction mixtures contained in a final volume of 25  $\mu\text{L}$ : 300  $\mu\text{M}$  R1 (pre-reduced), 300  $\mu\text{M}$  R2, 1.0 mM TTP, 0.8 mM NADPH, 20  $\mu\text{M}$  TR, 1  $\mu\text{M}$  TRR, and 1.0 mM either  $3'$ - $^{16}\text{O}$ - or  $3'$ - $^{17}\text{O}$ - $\text{N}_3\text{UDP}$  in 50 mM HEPES (pH 7.6), 15 mM  $\text{MgSO}_4$ , and 1 mM EDTA. All components of the reaction mixture except for the inhibitor were combined and incubated at 25 °C for 5 min. The reaction was started by the addition of inhibitor, and the mixture was drawn into suprasil capillaries by capillary action and frozen in liquid nitrogen 5 min after initiation. Spectra were acquired at 70 K on a custom-designed pulsed spectrometer.<sup>36</sup> The stimulated echo sequence<sup>37</sup> was used with a pulse length of  $t_{\pi/2} = 60$  ns and a pulse spacing of  $\tau = 200$  ns. The pulsed method allowed us to filter out the  $\text{N}\bullet$  radical signal from the  $\text{Y}\bullet$ , as we previously demonstrated with the reaction of  $3'$ - $^{16}\text{O}$ - $\text{N}_3\text{UDP}$ .<sup>38</sup> The external magnetic field was swept with the assistance of a field lock described elsewhere.<sup>39</sup> The echo intensity at each field position was integrated, and an average of 1000 shots per point was taken. The number of scans and recycle delays were adjusted for different signal intensities and temperatures.

**Simulations of the EPR Spectra.** The simulations were performed using the commercial software package SimFonia (Bruker). As a control, the  $\text{N}\bullet$  spectrum observed in the reaction of  $3'$ - $^{16}\text{O}$ - $\text{N}_3\text{UDP}$  with RNR was first simulated using the parameters reported by van der Donk et al.,<sup>30</sup> that is,  $g_{xx} = 2.01557$ ,  $g_{yy} = 2.00625$ ,  $g_{zz} = 2.00209$ ,  $A_{xx}(^{14}\text{N}) = 2$  G,  $A_{yy}(^{14}\text{N}) = 2$  G,  $A_{zz}(^{14}\text{N}) = 31$  G,  $A_{xx}(\text{H}) = A_{yy}(\text{H}) = A_{zz}(\text{H}) = 6.3$  G, and a Gaussian line shape broadening of 4.9 G (data not shown). The spectrum of  $\text{N}\bullet$  observed in the reaction of  $3'$ - $^{17}\text{O}$ - $\text{N}_3\text{UDP}$  with RNR was subsequently simulated by keeping the EPR

parameters for the unlabeled species fixed and varying the values of the  $^{17}\text{O}$  hyperfine tensor.

**Computational Methods.** The calculations for all model compounds were performed using unrestricted Kohn–Sham density functional theory (DFT) methods as implemented in GAUSSIAN 03<sup>40</sup> and TURBOMOLE.<sup>41</sup> Spin contamination effects were generally insignificant in all calculations. All structure optimizations were carried out with TURBOMOLE employing Becke's exchange functional B<sup>42</sup> and Perdew's P86<sup>43,44</sup> correlation functional together with the TZVP basis set<sup>45</sup> for all atoms and accelerated with the RI approximation using the standard TZVP auxiliary basis set from TURBOMOLE.<sup>46,47</sup>

For the computation of the hyperfine coupling (HFC) tensors with GAUSSIAN 03, a combination of Becke's three-parameter hybrid exchange functional B3<sup>48</sup> with the Perdew/Wang correlation functional PW91<sup>49,50</sup> was chosen. An ultrafine integration grid (58 410 integration points per atom) and standard SCF=Tight convergence criteria were applied. For these calculations, the Huzinaga–Kutzelnigg-type IGLO-II basis sets<sup>51</sup> were used for all atoms: (5s,1p)/[3s,1p] for H, (11s,7p,2d)/[7s,6p,2d] for S, and (9s,5p,1d)/[5s,4p,1d] for C, N, and O.

*Ab initio* calculations of HFC tensors were carried out at the coupled cluster theory level with single and double excitations and a perturbative treatment of triple excitations CCSD(T). The calculations were performed with the ACES II program<sup>52</sup> using unrestricted Hartree–Fock (UHF) reference wave functions. Spin densities were evaluated analytically from the CC relaxed density matrix.<sup>53–57</sup> IGLO-III basis

- (34) Chivers, P. T.; Prehoda, K. E.; Volkman, B. F.; Kim, B. M.; Markley, J. L.; Raines, R. T. *Biochemistry* **1997**, *36*, 14985–14991.  
 (35) Russel, M.; Model, P. *J. Bacteriol.* **1985**, *163*, 238–242.  
 (36) Bennati, M.; Farrar, C. T.; Bryant, J. A.; Inati, S. J.; Weis, V.; Gerfen, G. J.; Riggs-Gelasco, P.; Stubbe, J.; Griffin, R. G. *J. Magn. Reson., Ser. A* **1999**, *138*, 232–243.  
 (37) Hahn, E. L. *Phys. Rev.* **1950**, *80*, 580–594.  
 (38) Bennati, M.; Stubbe, J.; Griffin, R. G. *Appl. Magn. Reson.* **2001**, *21*, 389–410.  
 (39) Un, S.; Bryant, J.; Griffin, R. G. *J. Magn. Reson., Ser. A* **1993**, *101*, 92–94.

- (40) Frisch, M. J.; Trucks, G. W.; Schlegel, H. B.; Scuseria, G. E.; Robb, M. A.; Cheeseman, J. R.; Montgomery, J. A., Jr.; Vreven, T.; Kudin, K. N.; Burant, J. C.; Millam, J. M.; Iyengar, S. S.; Tomasi, J.; Barone, V.; Mennucci, B.; Cossi, M.; Scalmani, G.; Rega, N.; Petersson, G. A.; Nakatsuji, H.; Hada, M.; Ehara, M.; Toyota, K.; Fukuda, R.; Hasegawa, J.; Ishida, M.; Nakajima, T.; Honda, Y.; Kitao, O.; Nakai, H.; Klene, M.; Li, X.; Knox, J. E.; Hratchian, H. P.; Cross, J. B.; Bakken, V.; Adamo, C.; Jaramillo, J.; Gomperts, R.; Stratmann, R. E.; Zayzev, O.; Austin, A. J.; Cammi, R.; Pomelli, C.; Ochterski, J. W.; Ayala, P. Y.; Morokuma, K.; Voth, G. A.; Salvador, P.; Dannenberg, J. J.; Zakrzewski, V. G.; Dapprich, S.; Daniels, A. D.; Strain, M. C.; Farkas, O.; Malick, D. K.; Rabuck, A. D.; Raghavachari, K.; Foresman, J. B.; Ortiz, J. V.; Cui, Q.; Baboul, A. G.; Clifford, S.; Cioslowski, J.; Stefanov, B. B.; Liu, G.; Liashenko, A.; Piskorz, P.; Komaromi, I.; Martin, R. L.; Fox, D. J.; Keith, T.; Al-Laham, M. A.; Peng, C. Y.; Nanayakkara, A.; Challacombe, M.; Gill, P. M. W.; Johnson, B.; Chen, W.; Wong, M. W.; Gonzalez, C.; Pople, J. A. *Gaussian 03*, revision B.03; Gaussian, Inc.: Pittsburgh, PA, 2003.  
 (41) Ahlrichs, R.; Bär, M.; Baron, H.-P.; Bauernschmitt, R.; Böcker, S.; Deglmann, P.; Ehrig, M.; Eichkorn, K.; Elliott, S.; Furche, F.; Haase, F.; Häser, M.; Horn, H.; Hättig, C.; Huber, C.; Huniar, U.; Kattannek, M.; Köhn, A.; Kölmel, C.; Kollwitz, M.; May, K.; Ochsenfeld, C.; Öhm, H.; Schäfer, A.; Schneider, U.; Sierka, M.; Treutler, O.; Unterreiner, B.; von Arnim, M.; Weigend, F.; Weis, P.; Weiss, H. *TURBOMOLE*, version 5.6; Quantum Chemistry Group, University of Karlsruhe: Karlsruhe, Germany, 2002.  
 (42) Becke, A. D. *Phys. Rev. A* **1988**, *38*, 3098–3100.  
 (43) Perdew, J. P. *Phys. Rev. B* **1986**, *33*, 8822–8824.  
 (44) Perdew, J. P. *Phys. Rev. B* **1986**, *34*, 7406.  
 (45) Schäfer, A.; Huber, C.; Ahlrichs, R. *J. Chem. Phys.* **1994**, *100*, 5829–5835.  
 (46) Eichkorn, K.; Treutler, O.; Öhm, H.; Häser, M.; Ahlrichs, R. *Chem. Phys. Lett.* **1995**, *242*, 652–660.  
 (47) Eichkorn, K.; Weigend, F.; Treutler, O.; Ahlrichs, R. *Theor. Chem. Acc.* **1997**, *97*, 119–124.  
 (48) Becke, A. D. *J. Chem. Phys.* **1993**, *98*, 5648–5652.  
 (49) Perdew, J. P.; Wang, Y. *Phys. Rev. B* **1992**, *45*, 13244–13249.  
 (50) Perdew, J. P. *Physica B* **1992**, *172*, 1–6.  
 (51) Kutzelnigg, W.; Fleischer, U.; Schindler, M.; Springer-Verlag: Heidelberg, Germany, 1990; Vol. 23, p 165ff.  
 (52) ACES II is a program product of the Quantum Theory Project, University of Florida. Authors: Stanton, J. F.; Gauss, J.; Watts, J. D.; Nooijen, M.; Oliphant, N.; Perera, S. A.; Szalay, P.; Lauderdale, W. J.; Kucharski, S. A.; Gwaltney, S. R.; Beck, S.; Balkova, A.; Bernholdt, D. E.; Baeck, K. K.; Rozyczko, P.; Sekino, H.; Huber, C.; Pittner, J.; Bartlett, R. J. Integral packages included are VMOL (Almlöf, J.; Taylor, P. R.), VPOROS (Taylor, P. R.), and ABACUS (Helgaker, T.; Jensen, H. J. A.; Jørgensen, P.; Olsen, J.; Taylor, P. R.).  
 (53) Gauss, J.; Stanton, J. F.; Bartlett, R. J. *J. Chem. Phys.* **1991**, *95*, 2639–2645.  
 (54) Gauss, J.; Lauderdale, W. J.; Stanton, J. F.; Watts, J. D.; Bartlett, R. J. *J. Chem. Phys. Lett.* **1991**, *182*, 207–215.  
 (55) Watts, J. D.; Gauss, J.; Bartlett, R. J. *J. Chem. Phys. Lett.* **1992**, *200*, 1–7.  
 (56) Watts, J. D.; Gauss, J.; Bartlett, R. J. *J. Chem. Phys.* **1993**, *98*, 8718–8733.  
 (57) Perera, S. A.; Watts, J. D.; Bartlett, R. J. *J. Chem. Phys.* **1994**, *100*, 1425–1434.

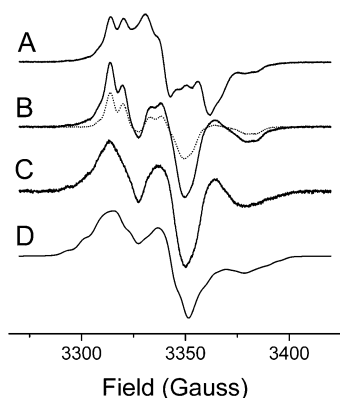


**Figure 3.** X-band EPR spectra of the  $\text{N}\bullet$  formed during inhibition of RNR by  $3'-[^{17}\text{O}]\text{-N}_3\text{UDP}$ . (A)  $3'-[^{17}\text{O}]\text{-N}_3\text{UDP}$  was incubated with RNR as described in Materials and Methods. The spectrum is a composite of the signals from the  $\text{Y}\bullet$  and the  $\text{N}\bullet$ . (B) Spectrum of the  $\text{N}\bullet$  generated in the presence of  $46 \pm 2\%$  enriched  $3'-[^{17}\text{O}]\text{-N}_3\text{UDP}$  (solid line) and  $3'-[^{16}\text{O}]\text{-N}_3\text{UDP}$  (dashed line) after subtraction of the  $\text{Y}\bullet$  (35.9% of the  $\text{Y}\bullet$  standard). The resulting  $3'-[^{16}\text{O}]\text{-N}_3\text{UDP}$  spectrum (dashed line) was scaled to 54%. (C) Spectrum of the  $3'-[^{17}\text{O}]\text{-N}_3\text{UDP}$  component of the spectrum in (B) after subtraction of the contribution from the  $[^{16}\text{O}]\text{-labeled}$  material (dashed line in B), and (D) simulation of the resulting spectrum with the parameters given in the text. Acquisition parameters are listed in the Materials and Methods.

sets<sup>51</sup> were employed for all atoms: (6s,2p)/[4s,2p] for H, (12s,8p,3d)/[8s,7p,3d] for S, and (11s,7p,2d)/[7s,6p,2d] for C, N, and O. The small model systems for these calculations were created by cutting out the relevant parts of the larger structurally optimized models and adding hydrogen atoms with standard bond lengths and angles to satisfy the open valences. No further structure optimizations were performed for these substructures.

## Results

Our previous studies suggested two possible structures for the  $\text{N}\bullet$  observed during the inactivation of *E. coli* RNR by  $\text{N}_3\text{-NDPs}$  (**6** and **7**, Figure 2). To distinguish between these options,  $46 \pm 2\%$  enriched  $3'-[^{17}\text{O}]\text{-N}_3\text{UDP}$  was prepared.<sup>31</sup> In a control experiment, this compound caused time-dependent inactivation of R1 and R2 that was identical to that observed with  $3'-[^{16}\text{O}]\text{-N}_3\text{UDP}$ . Incubation of  $3'-[^{17}\text{O}]\text{-N}_3\text{UDP}$  with R1 and R2 in the presence of effector TTP for 5 min followed by freezing in liquid nitrogen gave the X-band CW EPR spectrum shown in Figure 3.

The X-band CW EPR spectrum in Figure 3A is a composite of the  $\text{Y}\bullet$  and the  $\text{N}\bullet$  radicals. The contribution to the spectrum from the  $\text{Y}\bullet$  (35.9%  $\text{Y}\bullet$ ) was subtracted, giving the spectrum shown in Figure 3B. This spectrum represents contributions from  $[^{16}\text{O}]\text{-}$  and  $[^{17}\text{O}]\text{-labeled}$  nucleotide in the ratio of 54:46. Subtraction of the contribution from the  $[^{16}\text{O}]\text{-labeled}$  material (shown in Figure 3B with a dashed line) resulted in the spectrum of  $[^{17}\text{O}]\text{-N}\bullet$  shown in Figure 3C. The observed spectrum exhibits considerable hyperfine broadening on its low-field features. Simulation of the spectrum (Figure 3D) reveals a  $[^{17}\text{O}]\text{ hyperfine}$  tensor with  $|A_{xx}| = 8.5$  G,  $|A_{yy}| = 1.5$  G,  $|A_{zz}| = 1.0$  G and Euler angles  $\alpha = 0^\circ$ ,  $\beta = 27^\circ$ , and  $\gamma = 0^\circ$  with respect to the g-tensor principal axes. As a control, we also performed simulations with a home-written CW EPR fit program, and we obtained similar  $[^{17}\text{O}]\text{ HFC}$  values,  $|A_{xx}| = 7.6$  G,  $|A_{yy}| = 0.0$  G, and  $|A_{zz}| = 0.1$  G (see Supporting Information). The spread in these values provides an estimate of the error involved, likely  $\pm 1$  G. From the principal HFC values, we can separate the isotropic ( $A_{\text{iso}}$ ) from the anisotropic ( $T_{\text{diag}}$ ) part of the tensor.

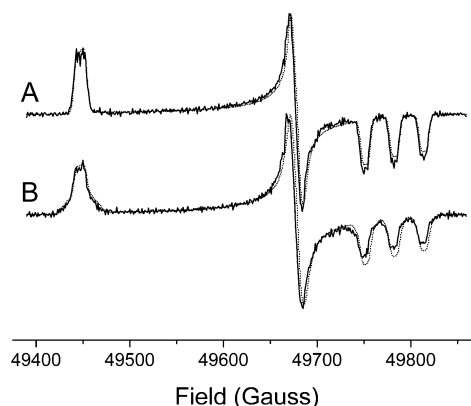


**Figure 4.** Derivative line shapes of the 140 GHz pulsed EPR spectra of  $\text{N}\bullet$ . (A)  $\text{N}\bullet$  formed during inhibition of RNR with  $3'-[^{16}\text{O}]\text{-N}_3\text{UDP}$ . (B)  $\text{N}\bullet$  formed during inhibition of RNR with 46% enriched  $3'-[^{17}\text{O}]\text{-N}_3\text{UDP}$ . The spectrum is a composite of the signals from  $[^{16}\text{O}]\text{-N}\bullet$  (shown in A) and  $[^{17}\text{O}]\text{-N}\bullet$  in the 54:46 ratio. Simulations are plotted as dashed lines on top of the experimental spectra, and simulation of B represents the sum of the weighted contributions of  $[^{16}\text{O}]\text{ and } [^{17}\text{O}]\text{ material}$ . Acquisition parameters are listed in Materials and Methods. Spectra were normalized with respect to the center line.

Since the signs of the tensor components are unknown, we distinguish two cases: one in which all tensor components have the same sign, and the second in which the two smaller components,  $A_{xx}$  and  $A_{yy}$ , which are almost equal, have an opposite sign from  $A_{zz}$ . With  $A_{\text{iso}} = (A_{xx} + A_{yy} + A_{zz})/3$  and  $T_{\text{diag}} = (A_{xx}, A_{yy}, A_{zz}) - A_{\text{iso}}$ , we obtain in the first case  $A_{\text{iso}} = -3.7$  G and  $T_{\text{diag}} = (-4.8, 2.2, 2.7)$  G, and in the second case  $A_{\text{iso}} = -2.0$  G and  $T_{\text{diag}} = (-6.5, 3.5, 3.0)$  G. We note that the signs of all the HFC constants are not absolute but relative to each other.

**High-Field EPR.** A similar set of inactivation experiments was carried out and  $\text{N}\bullet$  examined by 140 GHz EPR spectroscopy. The derivatives of the echo-detected spectra are shown in Figure 4. Here, the spectra do not contain contributions from  $\text{Y}\bullet$  because of the pulsed acquisition method employed. A comparison of the spectrum of  $\text{N}\bullet$  derived from  $3'-[^{17}\text{O}]\text{-N}_3\text{UDP}$  (Figure 4B) with the spectrum derived from  $3'-[^{16}\text{O}]\text{-N}_3\text{UDP}$  (Figure 4A) reveals a visible broadening of the low-field portion of the spectrum relative to the high-field portion. The magnitude of the broadening could be simulated using the same parameters as those used for the simulation of the 9 GHz data (Figure 4, dashed lines).

**Quantum Chemical Calculations to Assign the Structure of  $\text{N}\bullet$ .** Quantum chemical calculations have been performed to interpret the resulting EPR parameters and to distinguish between **6** and **7** (Figure 2). To make the calculations tractable, models of  $\text{N}\bullet$  were generated in which the 5'-diphosphate group was removed and the nucleobase was replaced by an  $\text{NH}_2$  group (see Table 2). Finally, the C225 in the active site of R1 was represented by  $-\text{S}-\text{CH}_3$  or  $-\text{S}-\text{CH}_2\text{CH}_3$ . These models were structurally optimized without constraints to obtain the equilibrium geometries.

Before calculating the EPR parameters of these model compounds, *ab initio* coupled cluster (CCSD(T)) calculations were carried out for smaller substructures to evaluate the validity of the DFT methods in predicting the correct spin density distribution of radical structures such as **6** and **7**. Table 1 shows the HFC tensors for the small models obtained at CCSD(T) and DFT levels. Comparison of the constants revealed that influences

**Table 1.** Comparison between Isotropic ( $A_{\text{iso}}$ ) and Dipolar ( $T_{ij}$ ) Hyperfine Coupling Constants Obtained by UB3PW91/IGLO-II and IGLO-III and by *Ab initio* CCSD(T)/IGLO-III Calculations for Small Model Substructures of the Radical Structures ONS and CNS<sup>160</sup> (results for corresponding larger models are reported in Table 2 and Supporting Information) (all coupling constants in G)

		HO-N-SH (ONS-CUT)			HO-CH <sub>2</sub> -N-SH (CNS-CUT)		
		B3PW91 IGLO-II	B3PW91 IGLO-III	CCSD(T) IGLO-III	B3PW91 IGLO-II	B3PW91 IGLO-III	CCSD(T) IGLO-III
<sup>14</sup> N	$A_{\text{iso}}$	+9.43	+10.91	+14.56	+8.19	+9.16	+9.05
	$T_{11}$	-13.80	-14.05	-13.77	-11.41	-11.50	-10.30
	$T_{22}$	-12.90	-13.15	-12.94	-11.16	-11.27	-9.93
	$T_{33}$	+26.70	+27.20	+26.70	+22.57	+22.77	+20.23
<sup>17</sup> O	$A_{\text{iso}}$	-6.05	-6.35	-7.98	-3.46	-3.86	-5.87
	$T_{11}$	-20.34	-19.97	-17.90	-6.03	-5.96	-5.55
	$T_{22}$	+10.87	+10.65	+9.84	+3.16	+3.11	+2.55
	$T_{33}$	+9.47	+9.32	+8.07	+2.87	+2.85	+3.00

of basis set and method are almost negligible for the dipolar HFCs ( $T_{ij}$ ), whereas the isotropic HFC constants ( $A_{\text{iso}}$ ) showed some dependence on both. DFT calculations, in particular the computations employing the IGLO-II basis set, systematically slightly underestimated the [<sup>14</sup>N] and [<sup>17</sup>O] isotropic HFC constants. For ONS-CUT (the name represents the structure as defined in Table 1), the deviation between DFT and CCSD(T) [<sup>14</sup>N] isotropic HFC constants is up to about 5 G, but for CNS-CUT, the deviation is only 0.9 G. On the other hand, the effect on the [<sup>17</sup>O] isotropic HFC constant is more pronounced for the CNS-CUT model. These trends must be considered when comparing the results of calculations with the experimental data. Nevertheless, the *ab initio* validation study shows that the DFT computations employing the IGLO-II basis set yield satisfying spin densities and HFC constants for the systems under study, even though the Fermi contact contributions may be underestimated.

After method validation, the EPR parameters for the larger freely geometry optimized model systems ONS, ONS\*, and CNS (see Table 2) were computed. For completeness, the proposed oxygen- and carbon-centered precursor radicals to N• (10 and 11 in Figure 2, see also CNS-O in Table 2) were also included in the theoretical study. The carbon-centered radical resulting from the sulfinylimine radical attack on the oxygen of the ketone ( $\bullet\text{C3}'\text{-O-NH-S-R}$ , 11, Figure 2) was not stable during structure optimization, collapsing back to the starting material. Pereira and co-workers recently reported a similar observation that the addition of the sulfinylimine to the 3'-oxygen is energetically highly disfavored.<sup>32</sup> The results for the oxygen-centered radical CNS-O (10, Figure 2), as well as for ONS, ONS\*, and CNS radicals, are shown in Table 2 together with the experimental data for N•. The CNS-O can immediately be ruled out by comparison of the experimental with the calculated HFC tensors; the calculated HFC constants are much smaller for [<sup>14</sup>N] and much larger for [<sup>17</sup>O] than the experimentally observed ones.

For all of the nitrogen-centered radicals (ONS, ONS\*, and CNS), the [<sup>14</sup>N] HFC tensors are in good agreement with experiment. Considering the systematic underestimation of the isotropic HFC tensors (see Table 1) which is more pronounced for the ONS-type structures, the CNS model seems to be in slightly better agreement with the experimental [<sup>14</sup>N] HFC tensor. A comparison of the [<sup>17</sup>O] HFC tensors allows us to rule out ONS-type structures (ONS or ONS\*) as candidates for N•. The direct bonding of the oxygen nucleus to the N• gives

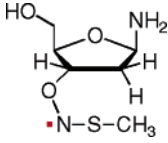
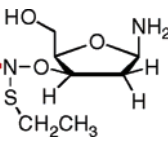
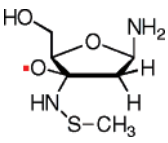
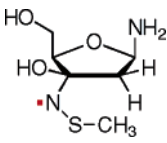
rise to [<sup>17</sup>O] HFC tensors much larger than those calculated for the CNS structures and those observed experimentally. This preliminary calculation with free structure optimization gave [<sup>17</sup>O] HFC constants for the CNS model that are smaller than the values found for N•, but suggested that this structure should be considered for further refinement.

**Further Refinement of the CNS Model.** The preceding analysis eliminates ONS models from further consideration. To ensure that the ONS-type structures can really be excluded, further calculations on various systematic side chain conformers of ONS and ONS\* were performed (data not shown). In all cases, the [<sup>17</sup>O] HFC tensors were similar to or even larger than those of the freely optimized structures (Table 2) and thus not in agreement with the experimental data. To find a better model for N•, focus was turned to CNS-type structures in which the orientation of the N-S-CH<sub>3</sub> side chain relative to the sugar ring was altered (Table 3). For these computations, the dihedral angle  $\varphi = \angle(\text{S-N-C3}'\text{-C4}')$  was set to a specific value and kept fixed during the structure optimizations, while all other degrees of freedom were allowed to fully relax. Freezing of the side chain orientation was done to mimic structural constraints imposed by the protein surroundings, in particular the positioning of the C225 side chain on the  $\alpha$  face of the sugar ring.<sup>58</sup> For the set of analyses from CNS<sub>180</sub> to CNS<sub>100</sub> (Table 3),  $\psi = \angle(\text{C}_{\text{CH}_3}\text{-S-N-C3}')$  was always close to 180°. The calculated [<sup>14</sup>N] and [<sup>17</sup>O] HFC tensors, selected distances, and molecular energies of the resulting conformers are shown in Table 3. For all structures in this series, the [<sup>14</sup>N] HFC constants agree well with the experimental data, whereas the [<sup>17</sup>O] HFC tensors and the N-H1' distances strongly depend on the structural model. In those cases where the [<sup>17</sup>O] HFC tensor is in reasonable accordance with the experiment (CNS<sub>160</sub>, CNS<sub>140</sub>, and CNS<sub>120</sub>), the distance between N• and the 1'-hydrogen appears too large compared to the experimental ESEEM values,<sup>29,30</sup> that is, the sugar ring is in a different conformation. To create a model that addresses this discrepancy, a calculation with an additional N-H1' distance constraint was performed (CNS\*<sub>140</sub> in Table 3). Here, the sugar ring conformation and the N-H1' distance were taken from the CNS equilibrium model (CNS,  $r(\text{N-H1}') = 3.33 \text{ \AA}$ ), and the side chain dihedral angle  $\varphi = 140^\circ$  was taken from the model exhibiting the best agreement of the [<sup>17</sup>O] HFC tensor (CNS<sub>140</sub>). The fixed N-H1' distance represents potential constraints imposed on the sugar conformation by the protein in the active site of RNR. Using these two structural constraints, the model displayed in Figure 5 was obtained in good agreement with experimental data (Table 3). The model also accounts for the fact that the Cys225 residue is located below the sugar ring. Furthermore, the energy difference between the CNS\*<sub>140</sub> model and the CNS equilibrium structure (CNS) amounts to only 2.5 kcal/mol, a value reasonably small to represent structural influences of the protein surroundings on the geometry of N•. Therefore, the CNS\*<sub>140</sub> structure (Figure 5) represents our best model for N•. The model requires that the C1'-H1' and C3'-N bonds are oriented almost axially relative to the plane of the sugar ring defined by C1', C3', and C4' and that the N-S-CH<sub>3</sub> side chain possesses a conformation that leads to an orientation of the p<sub>z</sub>-type nitrogen orbital toward the 3'-oxygen.

(58) Uhlin, U.; Eklund, H. *Nature* **1994**, *370*, 533–539.

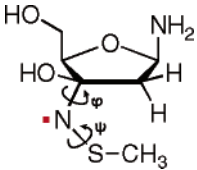


**Table 2.** Calculated Hyperfine Coupling Tensors and Selected N–H Distances of Structural Models of the N• Radical after Free Structure Optimization. HFC Tensors were Computed on the UB3PW91/IGLO-II Level of Theory (all coupling constants are in G, and all distances are in Å)

						exp <sup>b</sup>
		ONS	ONS* <sup>a</sup>	CNS-O	CNS	
<sup>14</sup> N	$A_{\text{iso}}$	+8.90	+8.89	-0.61	+7.39	+9.0/+11.7
	$A_{xx}$	-3.99	-4.45	-3.27	-3.92	-/+2.0
	$A_{yy}$	-3.21	-3.44	-3.07	-3.70	-/+2.0
	$A_{zz}$	+33.90	+34.56	+4.51	+29.79	+/+31.0
<sup>17</sup> O	$A_{\text{iso}}$	-6.64	-6.69	-5.67	-0.94	-2.0/-3.7
	$A_{xx}$	-25.63	-26.35	-48.55	-2.44	-/-8.5
	$A_{yy}$	+3.52	+3.93	+15.88	-0.26	+/-1.5
	$A_{zz}$	+2.20	+2.34	+15.67	-0.12	+/-1.0
$r(\text{N}-\text{H}1')$	4.07	5.17	4.54	3.33	3.0(2)	
$r(\text{N}-\text{H}4')$	3.72	4.51	2.53	2.36	2.7(3)	

<sup>a</sup> The N–O–C3'–C4' dihedral angle was set to 180° and held constant for this model. <sup>b</sup> The error of the experimental HFC constants was estimated to be ±1 G (see Results). For the HFC tensors, two cases for the relative signs of the  $A_{ii}$  components are shown together with the two corresponding  $A_{\text{iso}}$  values (see Results).

**Table 3.** Hyperfine Coupling Tensors, Molecular Energies, and Selected N–H Distances for Different Conformers of the CNS Model. In Most Cases, the Dihedral Angle  $\varphi = \angle(\text{S}-\text{N}-\text{C}3'-\text{C}4')$  was Frozen during Structure Optimizations. Angles Given in Brackets Were Freely Optimized. HFC Tensors Were Computed on the UB3PW91/IGLO-II Level of Theory (all coupling constants in G, distances in Å, and energies in Hartree)

			CNS	CNS <sub>180</sub>	CNS <sub>160</sub>	CNS <sub>140</sub>	CNS <sub>120</sub>	CNS <sub>100</sub>	CNS* <sub>140</sub> <sup>a</sup>	exp <sup>b</sup>
			( $\varphi = 203^\circ$ ) ( $\psi = 186^\circ$ )	$\varphi = 180^\circ$ ( $\psi = 183^\circ$ )	$\varphi = 160^\circ$ ( $\psi = 176^\circ$ )	$\varphi = 140^\circ$ ( $\psi = 174^\circ$ )	$\varphi = 120^\circ$ ( $\psi = 182^\circ$ )	$\varphi = 100^\circ$ ( $\psi = 183^\circ$ )	$\varphi = 140^\circ$ ( $\psi = 173^\circ$ )	
<sup>14</sup> N	$A_{\text{iso}}$		+7.39	+7.12	+7.59	+7.90	+8.14	+8.22	+7.82	+9.0/+11.7
	$A_{xx}$		-3.92	-4.01	-3.50	-3.40	-3.34	-3.29	-3.72	-/+2.0
	$A_{yy}$		-3.70	-3.79	-3.32	-3.25	-3.24	-3.17	-3.57	-/+2.0
	$A_{zz}$		+29.79	+29.16	+29.60	+30.35	+31.00	+31.12	+30.74	+/+31.0
<sup>17</sup> O	$A_{\text{iso}}$		-0.94	-0.91	-1.55	-2.56	-1.44	-0.43	-2.27	-2.0/-3.7
	$A_{xx}$		-2.44	-4.69	-6.94	-8.63	-6.37	-3.14	-8.80	-/-8.5
	$A_{yy}$		-0.26	+0.88	+1.04	+0.37	+0.94	+0.87	+0.88	+/-1.5
	$A_{zz}$		-0.12	+1.08	+1.24	+0.58	+1.11	+0.98	+1.11	+/-1.0
$r(\text{N}-\text{H}1')$		3.33	3.59	4.55	4.58	3.97	3.87	3.33 <sup>a</sup>	3.0(2)	
$r(\text{N}-\text{H}4')$		2.36	2.37	2.44	2.46	2.49	2.49	2.34	2.7(3)	
energy			-969.64611	-969.64477	-969.64579	-969.64504	-969.64165	-969.64141	-969.64206	

<sup>a</sup> The asterisk denotes that the N–H1' distance was set to a value of 3.33 Å and kept fixed during the structure optimization of this model. <sup>b</sup> The error of the experimental HFC constants was estimated to be ±1 G (see Results). For the HFC tensors, two cases for the relative signs of the  $A_{ii}$  components are shown together with the two corresponding  $A_{\text{iso}}$  values (see Results).

Further calculations of the conformational study also included a systematic variation of the  $\psi = \angle(\text{C}_{\text{CH}_3}-\text{S}-\text{N}-\text{C}3')$  angle (see Supporting Information). These results reveal that an alteration of this dihedral angle has a much smaller influence on the [<sup>17</sup>O] HFC tensor than the variation of  $\varphi$ , but that it leads to a considerable increase of the [<sup>14</sup>N] HFC constants when the C3'–N and the S–CH<sub>3</sub> bonds approach a perpendicular arrangement with respect to each other ( $\psi$  close to 90 or 270°).

## Discussion

Previous studies by van der Donk et al.<sup>30</sup> suggested two possible structures for N• generated during inactivation of class I RNRs with N<sub>3</sub>NDPs. The experimental data allowed **7** to be favored over **6**, although generation of **7** and its decomposition

to furanone **12** were mechanistically difficult to rationalize (Figure 2). Recently, pathways for generation of **6** and **7** (Figure 2) have been considered theoretically.<sup>32</sup> Structure **6** was favored energetically and an alternative pathway for its production proposed. To distinguish between **6** and **7**, 46% enriched [<sup>17</sup>O]-N<sub>3</sub>UDP was synthesized,<sup>31</sup> the resulting N• examined by EPR spectroscopy, and quantum chemical calculations were carried out to reproduce the experimental HFC tensors.

The 9 and 140 GHz EPR spectra of the N• radical generated with [<sup>17</sup>O]-N<sub>3</sub>UDP show substantial hyperfine broadening at the low-field side, indicating that the [<sup>17</sup>O] nucleus at the 3'-position is located close to the nitrogen-centered radical, as expected from the proposed structures **6** and **7**. To our knowledge, there



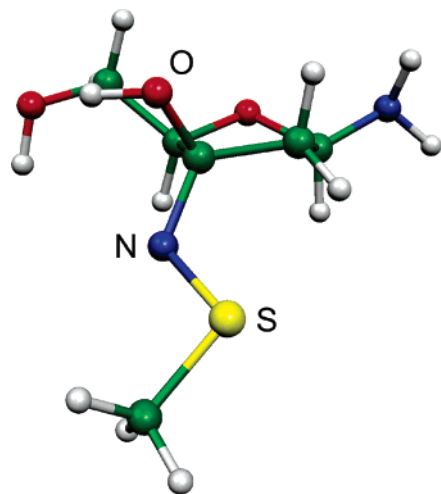


**Figure 5.** Structure of the N• radical with the CNS\*<sub>140</sub> conformation as obtained from the quantum chemical calculations.

is no information in the literature on hyperfine couplings of R–[<sup>17</sup>O]–N•–S–R- or H–[<sup>17</sup>O]–C–N•–S–R-type radicals. Thus, it was not feasible to distinguish between **6** and **7** solely based on direct comparison of the observed [<sup>17</sup>O] hyperfine tensor ( $|A_{xx}| = 8.5$  G,  $|A_{yy}| = 1.5$  G,  $|A_{zz}| = 1.0$  G) with literature data.

To get more insight into the structure of this unusual radical and into the mechanism of the [<sup>17</sup>O] hyperfine coupling, we employed DFT calculations. The DFT method was first validated by *ab initio* CCSD(T) calculations on small model systems of the ONS and CNS radical structures and then applied to the radical structures **6** and **7**. The DFT calculations clearly ruled out the ONS structure **7**, as this structure requires a much larger [<sup>17</sup>O] hyperfine coupling than is observed experimentally.

The calculations for the CNS-type structures resulted in much smaller HFC tensor components than for ONS-type structures. A critical dependence of the [<sup>17</sup>O] HFC on the conformation of the side chain connecting the protein to the plane of the sugar ring determined by C1', C3', and C4' could be observed. A rotation of this side chain into a position in which the S–CH<sub>3</sub> points below and almost perpendicular to the sugar ring plane (the CNS\*<sub>140</sub> model) leads to [<sup>17</sup>O] HFC tensors in good agreement with the experimental data. These results have now allowed us to qualitatively rationalize the mechanism of the [<sup>17</sup>O] HFC and the substantial value of  $A_{\text{iso}}$ . Since the main portion of spin density in N• is localized in the  $p_z$ -orbitals of the nitrogen and sulfur, rotation of the side chain can produce overlap between the nitrogen  $p_z$ -orbital and the  $p_z$ -orbital of the 3'-oxygen for some specific conformations, inducing spin density at the [<sup>17</sup>O] nucleus. The situation is best illustrated in Figure 6, where the calculated spin density distribution is displayed for two different side chain conformations.

Additionally, we compared the geometry of the CNS\*<sub>140</sub> structure with the distances between the nitrogen-centered radical and the protons at the 1'-, 2'-, and 4'-positions of the sugar ring determined from ESEEM studies.<sup>29,30</sup> On the basis of these data, the distance between N• and the 1'-<sup>2</sup>H was determined to be 3.0 Å and the distance between N• and the 4'-<sup>2</sup>H was determined to be 2.7 Å. The interaction of N• with the 2'-<sup>2</sup>H in a selectively deuterated sample (<sup>2</sup>H is on the  $\beta$  face) could not be detected by ESEEM. The DFT results reproduce these experimental distances reasonably well when

the sugar ring assumes the conformation shown in Figure 5. The energy of the CNS\*<sub>140</sub> structure was found to be only 2.5 kcal/mol above the equilibrium structure (CNS, Table 3), which can be reasonably attributed to constraints posed either by the large substituents of the sugar ring (not taken into account in the calculation) or by the active site. In the optimized structure of Figure 5, the distance to the 2'-hydrogen on the  $\beta$  face is 3.42 Å. The DFT calculations yield dipolar HFCs to the 1'-, 2'- ( $\beta$  face), and 4'-deuterons of  $T_{\perp}(1'^{-2}\text{H}) = -0.09$  G,  $T_{\perp}(2'^{-2}\text{H}) = -0.07$  G, and  $T_{\perp}(4'^{-2}\text{H}) = -0.23$  G. The 2'-<sup>2</sup>H HFC constant is the smallest one among the couplings to the three deuterons. This may be the reason why the interaction with the 2'-<sup>2</sup>H has not been detected in the ESEEM experiment.

Another parameter that can be used to confirm the reliability and accuracy of the computational results is the HFC to the protons on the  $\beta$ -carbon of the C225 residue. Experimentally, a splitting of 6.3 G was found in the X-band spectra that was assigned to a  $\beta$ -proton of C225.<sup>30</sup> The fact that only one of the two  $\beta$ -protons can be observed is due to the different orientation of the protons with respect to the p-type SOMO on sulfur and nitrogen leading to a large (6.3 G) and a small (<3 G) proton HFC. In our computational models, we have a methyl group instead of a methylene group at the position of the  $\beta$ -carbon of C225. For the CNS\*<sub>140</sub> model, the calculations yield hyperfine couplings to the three protons of  $A_{\text{iso}} = 6.7$  G and  $T_{\text{diag}} = (-1.1, -0.7, +1.8)$  G,  $A_{\text{iso}} = -0.6$  G and  $T_{\text{diag}} = (-0.9, -0.7, +1.6)$  G, and  $A_{\text{iso}} = 6.6$  G and  $T_{\text{diag}} = (-1.1, -0.7, +1.9)$  G, as well as dihedral angles  $\angle(\text{H}-\text{C}-\text{S}-\text{N})$  of  $-64.7$ ,  $+175.8$ , and  $+56.4^\circ$ , respectively. In all cases, the anisotropy of the coupling tensors is sufficiently small not to be resolved in the EPR spectra. The size of the HFC is in agreement with the experimental findings; the coupling is either close to 6.3 G or much smaller. It has to be noted here that the methyl group was allowed to freely relax in the structure optimizations of CNS\*<sub>140</sub>. It can be concluded that our favored model structure, CNS\*<sub>140</sub>, yields a spin density distribution which, together with the side chain orientation, is consistent with the  $\beta$ -proton HFC parameters of C225.

**Mechanistic Conclusions.** The EPR results in conjunction with DFT calculations that reproduce the observed HFC tensors provide strong support for the N• structure being best represented by **6**. The mechanism by which **6** is generated, however, is still not clear. Recent theoretical calculations suggested a mechanism that we had previously not considered, which is also presented in Figure 2.

Information collected over the past decade must be accounted for by any proposed mechanism. When N<sub>3</sub>UDP is incubated with RNR, a stoichiometric amount of 2-methylene-3-furanone **12**, inorganic pyrophosphate, and uracil are produced on a slow time scale (Figure 2) after N• breakdown. These products are proposed to result from nonenzymatic breakdown of the 3'-keto-2'-deoxynucleotide (**9**, Figure 2). Early in the time course of inactivation, the Y• on R2 is reduced. When 3'-[<sup>2</sup>H]-N<sub>3</sub>UDP is used in the reaction in place of the corresponding protonated material, there is an isotope effect on Y• loss, requiring hydrogen atom abstraction from C3'. The next step requires C2'–N bond cleavage based on isotopic labeling experiments using 2'-[<sup>13</sup>C]- and [<sup>15</sup>N]-N<sub>3</sub>UDP.<sup>29</sup> This process could occur either homolytically or heterolytically. We have favored the heterolytic mechanism based on studies with the normal substrate and 2'-

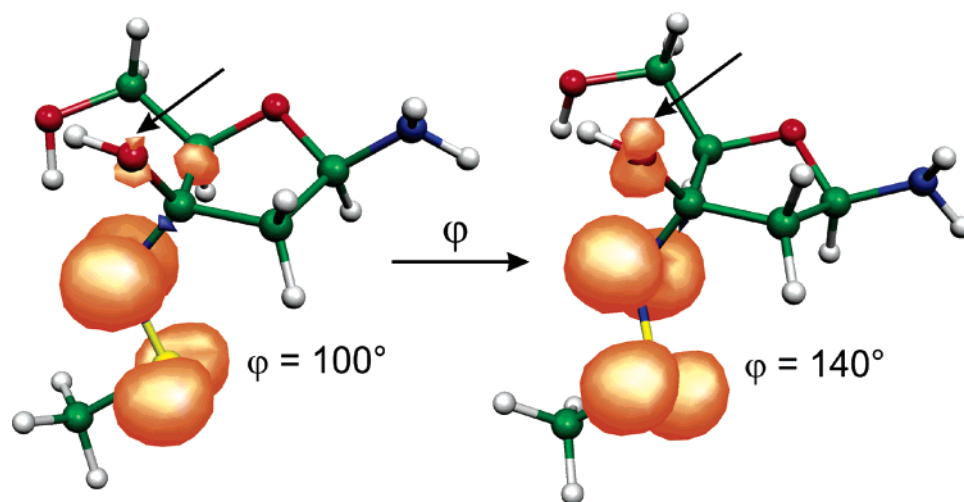


**Figure 6.** Plot of the spin density distribution for two different  $\varphi$  conformers (CNS<sub>100</sub> and CNS\*<sub>140</sub>) of the CNS-type model structure (isosensity cutoff value 0.0045 au). Rotation of the side chain about the N–C3' bond leads to a better overlap between the nitrogen p<sub>z</sub>-orbital and the p<sub>z</sub>-orbital of the 3'-oxygen for the  $\varphi = 140^\circ$  conformer, enabling a more efficient transfer of spin density from the nitrogen to the 3'-oxygen. Thus, one observes a larger 3'-oxygen spin density for the CNS\*<sub>140</sub> model. The arrows indicate the different spin densities at the 3'-oxygen for the two structures.

halogenated-2'-deoxynucleotides.<sup>1</sup> In our original mechanistic proposal, prior to the structural information,<sup>58</sup> the role of E441-R1 was not appreciated. Studies of the inactivation of RNR when E441 mutants of R1 were incubated with N<sub>3</sub>CDP revealed a greatly reduced rate of inactivation and slowed loss of Y•.<sup>59</sup> These results are similar to those observed when E441Q-R1 is incubated with CDP and support the proposal that E441 acts as a general base catalyst in the generation of ketyl radical **2** (Figure 2). Theoretical studies have been controversial about the role of E441, but recently, a consensus has been reached which agrees with model studies. Conversion of **5** to **2** (Figure 2) is proposed to be identical to the first few steps in the normal reduction process (Figure 1).<sup>60–62</sup>

The next step in our proposed mechanism, reduction of the ketyl radical **2** by proton-coupled electron transfer to generate the 3'-keto-2'-deoxynucleotide **3** (Figure 2), is also analogous to the proposed mechanism of reduction for CDP. This process leaves a thiyl radical in the active site. Evidence in support of steps **2** and **3** has been provided by mutational studies on C225 in R1 and more recently on N437 and E441 in R1.<sup>7,8,10,63,64</sup> Mutation of any of these residues results in rapid loss of Y•, but no N• is detected except in the case of E441D. In the case of C225S-R1, azide was observed (a distinction between azide and HN<sub>3</sub> is not possible based on the experimental method). In the case of N437Q- and E441Q-R1, the fate of the azide was not monitored. Thus, these groups involved in catalysis and/or maintaining the structural cavity in a conformation required for efficient nucleotide reduction (Figure 1), if altered, likely result in azide ion (or potentially HN<sub>3</sub>) release instead of being trapped by the thiyl radical. Reaction of hydrazoic acid within the active site by the thiyl radical is proposed to generate N<sub>2</sub>, which is produced stoichiometrically, and a sulfinylimine radical (**9**,

Figure 2) that has never been detected. It is unlikely that the thiyl radical would attack an azide ion. Thus, the protonated azide (pK<sub>a</sub> of 4.6) is essential for this mechanism.

The theoretical modeling study of Pereira et al.<sup>32</sup> generated an alternative, attractive, mechanistic proposal. The released azide ion blocks reduction by C225, and it is proposed to add to the 2'-ketyl radical **2** (Figure 2) concomitant with protonation of the ketone oxygen by E441. The resulting radical is subsequently reduced at the 2'-position by C225 to generate the C225 thiyl radical (**8**, Figure 2). Addition of azide to ketones has chemical precedent,<sup>65</sup> but to our knowledge, there are no model systems where azide adds to ketyl radicals. The attachment of azide to C3' would move it out of the way sterically and hence facilitate the reduction process. In this case, the attack of the thiyl radical is on an alkyl azide (instead of HN<sub>3</sub>), which has chemical precedence.<sup>66–68</sup>

In our mechanism, the sulfinylimine radical attacks the 3'-keto-2'-deoxynucleotide, generating an alkoxy radical (**10**, Figure 2) which abstracts a hydrogen atom from the NH to generate **6**. These two steps are unprecedented and we propose could occur because of the steric constraints within the active site cavity. The resulting radical is very stable, and its breakdown ultimately regenerates the 3'-keto-2'-deoxynucleotide that is proposed to dissociate from the active site and generate the observed products, furanone, inorganic pyrophosphate, and uracil (Figure 2).

In the theoretical model, the loss of N<sub>2</sub> occurs through thiyl radical (C225)-mediated reaction on **8** with direct generation of **6** (Figure 2). No mechanism for this process is described. The theoretical model further suggests that the breakdown of **6** to the 3'-keto-2'-deoxynucleotide involves E441-assisted hydrogen atom migration. How E441 could carry out this chemistry is unclear. At present, it is unlikely that one can experimentally distinguish between these two mechanistic models.

(59) Persson, A. L.; Eriksson, M.; Katterle, B.; Pötsch, S.; Sahlin, M.; Sjöberg, B. M. *J. Biol. Chem.* **1997**, *272*, 31533–31541.

(60) Siegbahn, P. E. M. *J. Am. Chem. Soc.* **1998**, *120*, 8417–8429.

(61) Himo, F.; Siegbahn, P. E. M. *J. Phys. Chem. B* **2000**, *104*, 7502–7509.

(62) Pelmenchikov, V.; Cho, K. B.; Siegbahn, P. E. M. *J. Comput. Chem.* **2004**, *25*, 311–321.

(63) van der Donk, W. A.; Zeng, C. H.; Biemann, K.; Stubbe, J.; Hanlon, A.; Kyte, J. *Biochemistry* **1996**, *35*, 10058–10067.

(64) Kasrayan, A.; Persson, A. L.; Sahlin, M.; Sjöberg, B.-M. *J. Biol. Chem.* **2002**, *277*, 5749–5755.

(65) Smith, P. A. S. *J. Am. Chem. Soc.* **1948**, *70*, 320–323.

(66) Kim, S.; Joe, G. H.; Do, J. Y. *J. Am. Chem. Soc.* **1994**, *116*, 5521–5522.

(67) Cartwright, I. L.; Hutchinson, D. W.; Armstrong, V. W. *Nucleic Acids Res.* **1976**, *3*, 2331–2339.

(68) Staros, J. V.; Bagley, H.; Standing, D. N.; Knowles, J. R. *Biochem. Biophys. Res. Commun.* **1978**, *80*, 568–572.

Structure **6** is very far removed in chemical space from the initial 3'-nucleotide radical (**1**, Figure 1). Furthermore, it is unlikely that a chemist could ever model this transformation given that it is uniquely associated with the active site cavity that has evolved to catalyze a very different reaction, nucleotide reduction, with exquisite precision. While N<sub>3</sub>NDPs are mechanism-based inhibitors of RNRs and thus the first few steps in the mechanism of reduction and inactivation are similar to the normal reduction reaction, after loss of water, the unique constellation of amino acid residues within the active site makes for unprecedented chemical transformations.

Understanding the normal mechanism of nucleotide reduction has been challenging. We have recently shown that a physical step prior to chemistry or radical initiation via electron transfer is rate-limiting.<sup>17</sup> Thus, we have had to use perturbants to study the mechanism: either substrate analogues or site-directed protein mutants. As argued above, we believe that this approach has been mechanistically informative about the normal mechanism of NDP reduction. We have interpreted our results of the N<sub>3</sub>NDP inactivation of RNR to suggest that we have evidence for the first time of the 3'-keto-2'-deoxynucleotide **3** (Figure 2) intermediate postulated to be involved in the normal reduction process or the 2'-ketyl radical **2** which is rapidly

converted to **3** (Figure 2). Thus, with identification of N• and our earlier studies, we presently have evidence for each step in the normal reduction process using either substrate or protein analogues. The story of the mechanism of inactivation of RNR by N<sub>3</sub>NDP has been a long one, which in the end has given us a great deal of insight into the catalytic capabilities of the complex protein and substrate-based radical mechanism of nucleotides to deoxynucleotides.

**Acknowledgment.** J.S. acknowledges the NIH Grant 29595. M.B. and J.F. acknowledge financial support by the DFG (SPP 1071 and SFB 472) and Prof. Prisner, as well as support by the Frankfurt Center for Scientific Computing. R.G. acknowledges the Grants EB002804 and EB002026.

**Supporting Information Available:** Alternative simulation of the X-band EPR spectrum of the 3'-[<sup>17</sup>O]-N<sub>3</sub>UDP component as well as calculated hyperfine coupling tensors and molecular energies for all CNS-type models that were included in the conformational studies. This material is available free of charge via the Internet at <http://pubs.acs.org>.

JA043111X